Nano Research

Open Access

Research Article

Stretchable artificial vision sensor with retinomorphic transistor-reservoir computing

Tongrui Sun[1,§], Xu Liu[1,§], Yutong Xu[1,§], Xinglei Zhao[2], Pu Guo[1], Junyao Zhang[1], Ziyi Guo[1], Yue Wu[1], Shilei Dai[1] ✉, and Jia Huang[1] ✉

[1] *School of Materials Science and Engineering, Tongji University, Shanghai 201804, China*
[2] *State Key Laboratory of Petroleum Pollution Control, Beijing, CNPC Research Institute of Safety and Environmental Technology, Beijing 102206, China*
[§] *Tongrui Sun, Xu Liu, and Yutong Xu contributed equally to this work.*

Cite this article: *Nano Research*, **2025**, *18*, 94907191. https://doi.org/10.26599/NR.2025.94907191

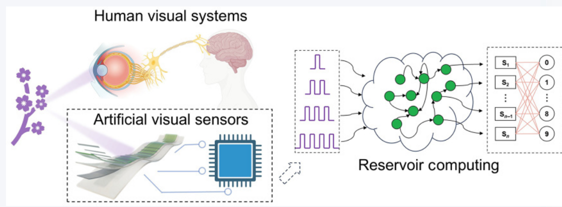

ABSTRACT: Artificial visual sensors (AVSs) with bio-inspired sensing and neuromorphic signal processing are essential for next-generation intelligent systems. Conventional optoelectronic devices employed in AVSs operate discretely in terms of sensing, processing, and memorization, and not ideal for applications necessitating shape deformation to achieve wide fields-of-view and deep depths-of-field. Here, we present stretchable artificial visual sensors (S-AVS) capable of concurrently sensing and processing optical signals while adapting to shape deformations. Specifically, these S-AVSs use a stretchable transistor structure with a meticulously engineered photosensitive semiconductor layer, comprising an organic semiconductor, thermoplastic elastomer, and cesium lead bromide quantum dots ($CsPbBr_3$ QDs). They exhibit synaptic behaviors such as excitatory postsynaptic current (EPSC) and paired-pulse facilitation (PPF) under optical signals, maintaining functionality under 30% strain and repeated stretching. The nonlinear response and fading memory effect support in-sensor reservoir computing, achieving image recognition accuracies of 97.46% and 97.1% at 0% and 30% strain, respectively.

KEYWORDS: stretchable electronics, artificial vision sensors (AVSs), retinomorphic transistors, reservoir computing, neuromorphic computing

1 Introduction

Artificial visual sensors (AVSs) play a vital role in driving advancements across various sectors including intelligent devices, autonomous driving, medical imaging, industrial automation, and security monitoring [1–4]. The predominant AVSs currently in use are based on either charge-coupled devices (CCDs) or complementary metal-oxide-semiconductor (CMOS) active-pixel sensors (APSs) [5–7]. While these sensors effectively capture visual data from the environment, they also produce a significant amount of redundant information [8]. This wealth of optical information is usually been converted into digital format and then transmitted to a computing unit for further processing. However, this transfer of large data volumes between the image sensor and processing unit results in delays (latency) and high-power consumption [9]. Moreover, CCDs and APSs are constructed using brittle materials on rigid substrates, hindering their ability to adaptively deform for achieving wide fields-of-view and deep depths-of-field during practical use [10]. Consequently, the necessity for complex multi-lens optics arises, leading to the development of bulky and heavy devices that compromise the overall mobility of the vision system. To overcome these challenges, a promising avenue is to emulate human visual systems by leveraging emerging optoelectronics (e.g., retinomorphic transistors) to develop next-generation AVSs [11–19]. These advanced AVSs would seamlessly integrate image acquisition and processing within a single device while incorporating stretchability through holistic materials innovation.

Up to date, numerous emerging optoelectronic devices have been designed to mimic the capabilities of the human visual system [20–24]. For instance, the mimicry of graded neurons' characteristics based on MoS_2 phototransistors, effectively encoding temporal light information [25]. Additionally, the emulation of striate cortex with binocular and orientation selectivity was achieved by $CsPbBr_2I$ memristors [26]. While these works emulate certain visual functions, they lack stretchable characteristics.

Received: July 4, 2024; **Revised:** October 18, 2024
Accepted: December 13, 2024

✉Address correspondence to Shilei Dai, sldai1@outlook.com; Jia Huang, huangjia@tongji.edu.cn

Although there have been some reports on stretchable neuromorphic vision sensors, only basic synaptic behaviors have been demonstrated, and none have shown the capability of implementing reservoir computing (RC) vision systems [27–31]. RC excels in efficiently processing temporal data and complex patterns with minimal training, making it ideal for tasks requiring real-time analysis and adaptive learning [32–34]. Implementing RC with stretchable AVSs is crucial for advanced visual signal processing but has not yet been realized.

In this study, we showcase a stretchable AVS (S-AVS) with a conventional phototransistor structure, showcasing its ability to implement a RC vision system (Fig. 1(a)). Specifically, our AVS comprises four stretchable components: (i) a stretchable photosensitive semiconductor film, (ii) stretchable sliver (Ag) metal-elastic polymer intermixing electrodes serving as both source-drain (S/D), and gate (G), (iii) an elastic dielectric layer, and (iv) an elastic substrate (Fig. 1(b)). The stretchable photosensitive semiconductor film is a rational designed ternary composite composed of the organic semiconductor poly[2,5-bis(2-octyldodecyl)pyrrolo[3,4-c]-pyrrole-1,4(2H,5H)-dione-3,6-diyl)-alt-(2,2';5',2'';5'',2'''-quaterthiophen-5,5'''-diyl)] (PDPP4T), the thermoplastic elastomer styrene-ethylene-butylene-styrene (SEBS), and cesium lead bromide quantum dots ($CsPbBr_3$ QDs) (Fig. 1(c)). Nanoconfinement of PDPP4T is attained by generating nanofibril aggregates within the SEBS matrix. This process not only improves the stretchability of PDPP4T but also maintains its charge transport properties (Fig. 1(d)) [35]. The inclusion of $CsPbBr_3$ QDs in the confined semiconductor film is due to their exceptional optical properties. Leveraging fading memory effect of AVSs can effectively emulate synaptic behaviors and enable in-sensor computing, particularly in in-sensor RC computing applications. Our experimental results demonstrate that our AVSs can well-mimic synaptic functions, including excitatory postsynaptic current (EPSC) and paired-pulse facilitation (PPF). These functionalities remain robust even under considerable deformation, enduring strains of up to 30% and repeated cycles of stretching. More importantly, our AVS-based RC vision systems achieve image recognition accuracies of 97.46% and 97.1% at 0% and 30% strain, respectively.

2 Experimental

2.1 Preparation of stretchable photosensitive semiconductor layer

PDPP4T (Hangzhou Order Science & Technology Co., Ltd.) and SEBS H1221 (Asahi Kasei) were dissolved in chlorobenzene (Energy Chemical) with a concentration ratio of 5:5 mg/mL at 80 °C overnight. Then, $CsPbBr_3$ QDs (Mesolight) and PDPP4T/SEBS solution were mixed at room temperature. Finally, the mixed solution was spin-coated onto the octadecyltrimethoxysilane (OTS) treated Si/SiO_2 substrate at 1000 rpm and annealed at 100 °C for 30 min in argon atmosphere. The Si/SiO_2 substrate was washed by sonication with acetone (Sinopharm) and isopropyl alcohol (Macklin). The OTS treated method was according to our previous report [36].

2.2 Preparation of S-AVS

The stretchable substrates were prepared by casting SEBS H1062 (200 mg/mL in toluene) onto glass slides to form elastic films. Stretchable G electrodes were prepared by evaporating 50 nm silver on SEBS substrates at a speed of 0.02 nm/s patterned by mask plates. The dielectric layer was prepared by spin coating SEBS H1052 solution (100 mg/mL in toluene) onto OTS treated Si wafer at 1000 rpm for 1 min and annealed at 70 °C for 20 min. Then, the polydimethylsiloxane (PDMS) elastomer was used to transfer SEBS dielectric layer and the semiconductor layer to SEBS substrate with the gate electrode. Finally, the evaporating S/D electrodes were prepared to form the final structure.

2.3 Characterization and measurements

The ultraviolet-visible (UV–vis) and the photoluminescence (PL) spectra of films were recorded by UH4150 and F-4700 spectrometers (Hitachi), respectively. The light microscopy was used to observe the stretchable film. The electrical properties of the photonic synapses were tested with PDA Fs-Pro in ambient conditions. The simulation of RC systems according to our previous report [37].

2.4 Simulation of RC systems

For the simulation of S-AVS-based RC system, firstly, S-AVS-based reservoir layer is utilized for information compression and preprocessing. The images of handwritten digits in MNIST are binarized first, and then trimmed to a size of 22 pixel × 20 pixel. Each row of an image is divided into five pulse sequences composed of 4 pixels containing "0" and "1", so an image can be converted into 22 × 5 = 110 pulse sequences, which are then input into the S-AVS-based reservoir layer to obtain the corresponding read currents. As a result, an image is coded into 110 read currents, which are then input into the backend fully connected neural network conducted by Python for later training and testing. The neural network consists of 110 input neurons, 150 hidden neurons, and 10 output neurons. There are 60,000 images used for training, and another 10,000 images are coded to test the classification accuracy.

3 Results and discussion

Before fabricating the S-AVS, we investigated the stretchability of a ternary composite of an organic semiconductor, which is the core component of S-AVS. Initially, we compared the stretchability of PDPP4T films with PDPP4T/SEBS composite films to evaluate the effect of SEBS on enhancing the stretchability of the composite semiconductor film. As shown in Fig. 1(d), the PDPP4T/SEBS film can be stretched to 100% strain without any cracks, while the pure PDPP4T film exhibited significant cracking at the same strain. This improved stretchability of the composite film can be attributed to the nanoconfinement effect [35]. Atomic force microscopy (AFM) was performed to investigate the detailed morphology of composite films. The PDPP4T/$CsPbBr_3$ and PDPP4T/$CsPbBr_3$/SEBS films with an average surface roughness (R_a) of ~ 4.3 and ~ 14 nm, respectively (Fig. 1(e)). To investigate the electrical performance of PDPP4T/SEBS films under strain, we fabricated organic thin-film transistors (OTFTs) on silicon wafers using stretched PDPP4T/SEBS composite films (Fig. S1 in the Electronic Supplementary Material (ESM)). The transfer curves of these transistors under different strains were similar to each other, demonstrating the potential of the PDPP4T/SEBS composite film as a semiconductor layer for stretchable transistors (Fig. 1(f)).

Based on the proven stretchability of PDPP4T/SEBS films, we tried to utilize the $CsPbBr_3$ QDs to enhance the photoresponsivity of the composite film. Firstly, we characterized the absorption spectra of PDPP4T and $CsPbBr_3$ QDs, respectively (Fig. 1(g)). The

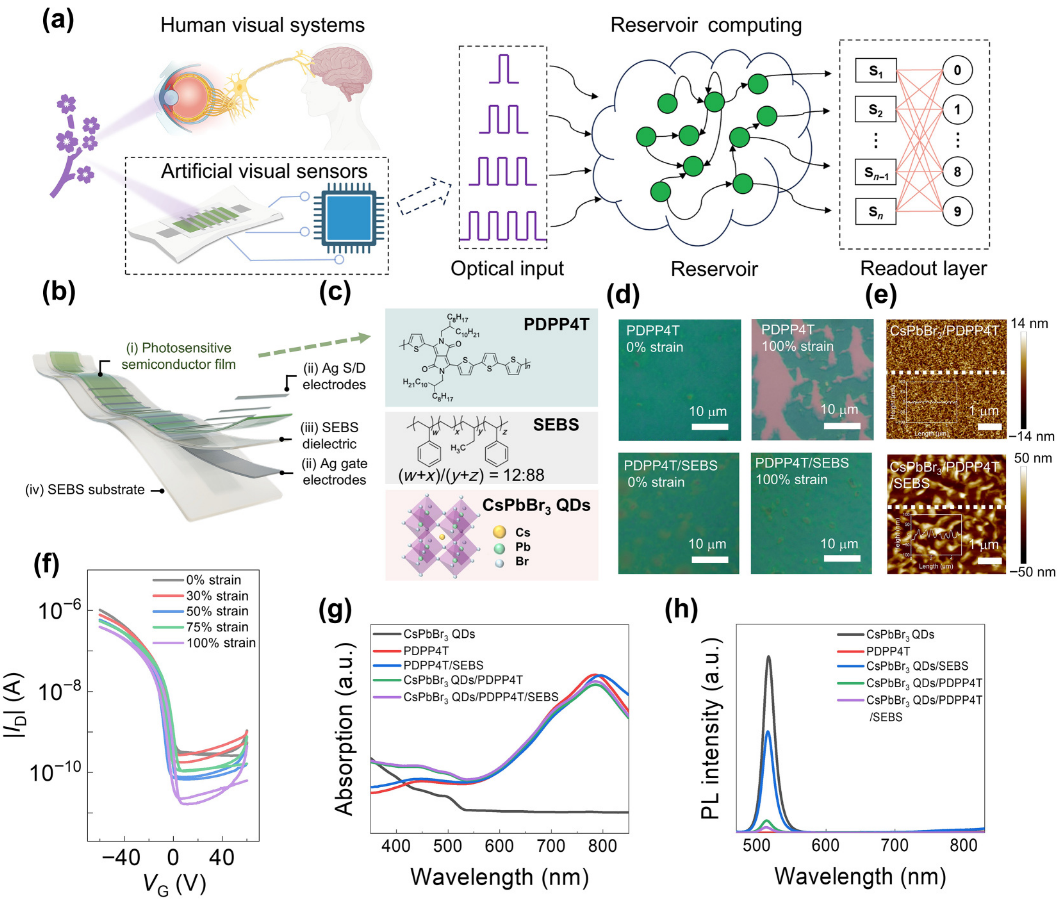

Figure 1 (a) Schematic illustration of the human visual system, AVS-RC system. (b) Device structure of S-AVS. (c) Chemical structures of semiconductor polymer PDPP4T, SEBS, and $CsPbBr_3$ QDs. (d) Optical micrograph of PDPP4T and PDPP4T/SEBS films at 0% and 100% strain. (e) AFM image of the $CsPbBr_3$ QDs/PDPP4T and $CsPbBr_3$ QDs/PDPP4T/SEBS hybrid film. Inset: the roughness profile of the film. (f) Transfer curves of PDPP4T/SEBS under different strains along the channel length direction. (g) The absorbance of the composite films. (h) PL measurement of the composite films. (Illustrations in (a) were created with BioRender.com)

pure PDPP4T film exhibits significant light absorption in the near-infrared region around 800 nm, and the $CsPbBr_3$ QDs predominantly absorb light at wavelengths below 500 nm, with a distinct absorption peak observed at 500 nm. Additionally, the combined absorption spectrum of the PDPP4T/$CsPbBr_3$ QDs composite film reveals simultaneous absorption peaks at both 800 and 500 nm. Notably, the addition of SEBS does not significantly alter the absorption spectra of the composite films (Fig. 1(g)). Furthermore, the steady-state photoluminescence was conducted to investigate the charge transfer efficiency between the $CsPbBr_3$ QDs, PDPP4T, and SEBS (Fig. 1(h)). The pure $CsPbBr_3$ QDs film exhibits a fluorescence peak, while PDPP4T shows no discernible fluorescence peak. Compared with the pure $CsPbBr_3$ QDs film, the fluorescence intensity of the $CsPbBr_3$ QDs/PDPP4T composite film significantly diminishes, indicating efficient charge transfer from $CsPbBr_3$ QDs to PDPP4T. Furthermore, we observed that the fluorescence intensity of the $CsPbBr_3$ QDs/SEBS binary composite film experiences a moderate reduction when compared to the $CsPbBr_3$ QDs film. Similarly, the ternary composite film $CsPbBr_3$ QDs/PDPP4T/SEBS also exhibits a certain degree of fluorescence attenuation relative to the $CsPbBr_3$ QDs/PDPP4T composite film, demonstrating the $CsPbBr_3$ QDs/PDPP4T/SEBS films have the highest photo-generated excitons separation efficiency.

Additionally, further investigation is required to explore the impact of introducing $CsPbBr_3$ QDs in PDPP4T/SEBS films on stretchability and photosensitivity. Under the premise that the mass ratio of PDPP4T to SEBS is 1:1, we prepared OTFTs based on ternary composite films with different concentration ratios of $CsPbBr_3$ QDs. The related light and dark transfer curves of OTFTs under different strains are shown in Fig. S2 in the ESM. It is observable that as the content of QDs moderately increases, the on-state current is reduced by around an order of magnitude, and the threshold of the device shifts to the positive voltage in light conditions. Furthermore, the current of all devices with solely stretched composite films degraded with the stretching degree. The key parameter for evaluating the light response capability, photoresponsivity (R), could be calculated by Eq. (1) [38]

$$R = \frac{I_{\text{light}} - I_{\text{dark}}}{PS} \quad (1)$$

where P is the light intensity per unit area, S is the channel area of the device, I_{light} is the photocurrent, and I_{dark} is the dark state current. The film with the mass ratio of $CsPbBr_3$ QDs:PDPP4T:SEBS = 0.3:1:1 showed the highest R value in either unstretched or stretched state (Fig. S3 in the ESM). In contrast, the film with the mass ratio of $CsPbBr_3$ QDs:PDPP4T:SEBS = 3:1:1 performed worse than the composite film without QDs, the possible reason could be attributed to the high-content QDs lowering the film quality (Fig. S4 in the ESM). AFM images were performed to investigate the uniformity and surface roughness of the $CsPbBr_3$ QDs/PDPP4T/SEBS hybrid film (Fig. S5 in the ESM). The $CsPbBr_3$ QDs/PDPP4T/SEBS hybrid film with an optimal blending ratio of 0.3:1:1 illustrated a homogeneous distribution of the $CsPbBr_3$ QDs in the hybrid matrix with R_a of ~ 14 nm. In contrast, the film with the mass ratio of $CsPbBr_3$ QDs:PDPP4T:SEBS = 3:1:1 performed shows the R_a of ~ 28 nm, the worse film could be attributed to the high-content QDs originating aggregate. As a result, we consider the $CsPbBr_3$ QDs:PDPP4T:SEBS ratio of 0.3:1:1 as the optimal ratio to fabricate the S-AVSs.

Building on the proven photosensitivity of the composite films, we further explored the light-driven synaptic properties of our device to assess its potential in mimicking the signal sensing and processing capabilities of biological eyes. Since our device is inherently a photosensor capable of detecting light signals, only the signal processing capability needed to be investigated. In biosystems, the signal processing is mainly conducted by synapses (Fig. 2(a)). Neurotransmitter-mediated synaptic plasticity forms the foundation for computing and memorization. When neurotransmitters reach the postsynaptic membrane, they alter its ionic permeability, resulting in changes in membrane potentials and currents [39–41]. Excitatory postsynaptic current (EPSC), generated by excitatory neurotransmitters, is a fundamental aspect of synaptic plasticity in biological synapses. We have successfully replicated EPSC behavior using our device, as shown in Fig. 2(b). Additionally, paired-pulse facilitation (PPF), another important form of synaptic plasticity induced by two consecutive presynaptic pulses, was effectively mimicked using our device with two consecutive optical pulses, as depicted in Fig. 2(c). By altering the interval between two pulses, we further studied the relative PPF characteristics by PPF index, which can be defined as follows (Eq. (2)) [42]

$$\text{PPF index} = \frac{A_2}{A_1} \times 100\% \qquad (2)$$

where A_1 and A_2 are the current values triggered by the first and the second light pulses. In Fig. 2(d), the PPF index decayed as the interval between the two pulses increased, which was consistent with the phenomena of biological synapses. As the intensity, duration, and repetition of optical pulse increased, the triggered EPSC increased concurrently, which simulated the conversion from short-term plasticity (STP) to long-term plasticity (LTP) (Figs. 2(e)–2(g)). The EPSC triggered by light pulses of different wavelengths is depicted in Fig. 2(h). Remarkably, the device current increased sharply once applying light pulses, and devices exhibited robust memory retention after pulses. The simulated photo-synaptic behavior demonstrates the device's capability for optical signal processing, which is highly essential for S-AVSs.

For the fully stretchable devices, all components, including electrodes, must be stretchable. We employed a thermal

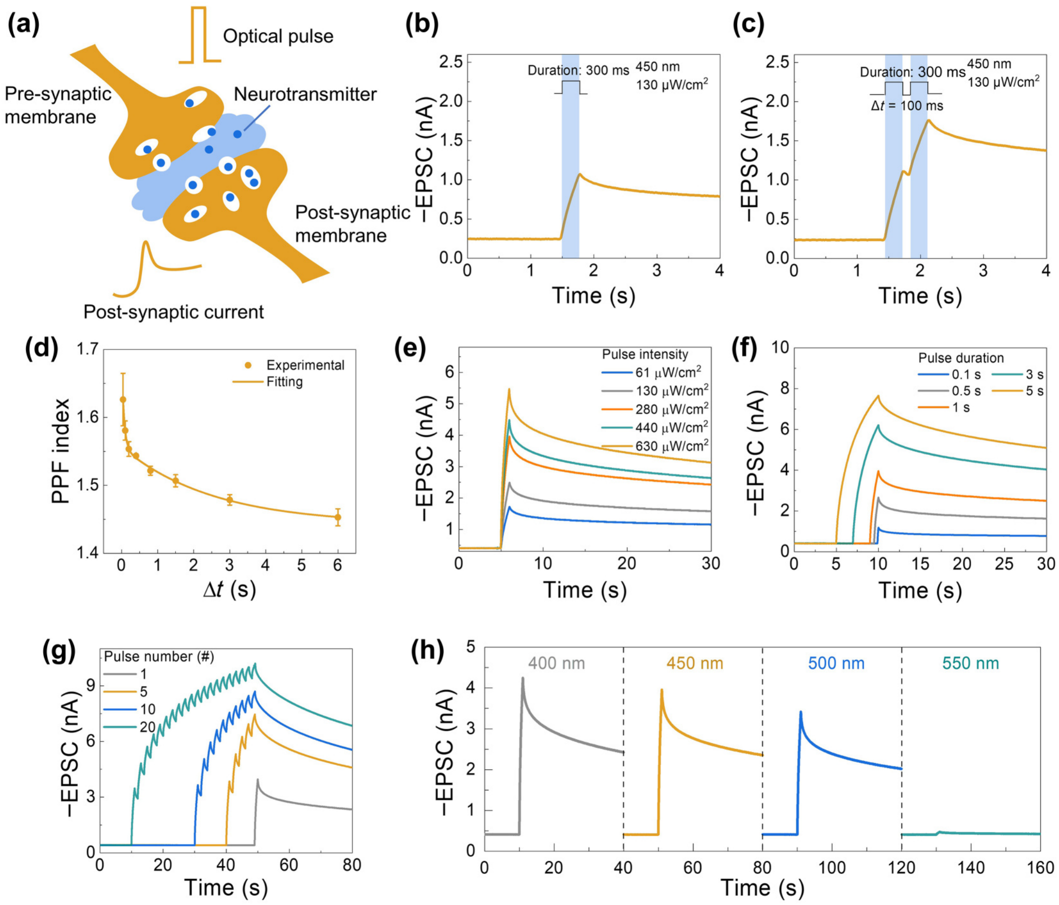

Figure 2 (a) Schematic diagram of a biological synapse. (b) EPSC behavior triggered by an optical pulse (130 μW/cm², 300 ms). (c) PPF behavior triggered by two consecutive optical pulses (130 μW/cm², 300 ms). (d) PPF index triggered by optical pulses (130 μW/cm², 300 ms) as a function of Δt. The simulation of conversion from STP to LTP is induced by increasing (e) intensity, (f) duration, and (g) pulse number. (h) EPSC behaviors triggered by the optical pulses with the wavelengths of 400, 450, 500, and 550 nm, respectively (280 μW/cm², 1 s)

evaporation method to deposited Ag onto SEBS substrate and the stretchable semiconductor layer to form stretchable G and S/D electrodes during S-AVSs fabrication. The stretchability of the electrodes is derived from the formation of an Ag-elastic polymer intermixing layer during thermal evaporation and the resistance change of Ag-elastic polymer electrodes under different strain states shown in Fig. S6 in the ESM. The intermixing layer significantly reducing the formation of large cracks on Ag electrodes during stretching [43]. Our devices feature a bottom-gate/top-contact configuration consisting of SEBS substrate, stretchable Ag-elastic polymer intermixing electrodes, SEBS dielectric, and photosensitive semiconductor layer (Fig. 3(a)). The self-adhesive SEBS components within the substrate, dielectric layer, and semiconductor film ensure a robust affinity between each part, preventing delamination during deformation. Optical photos in Fig. 3(b) demonstrate the mechanical robustness of our device during stretching, twisting, and poking. To investigate the impact of stretching on device performance, we conducted tests on the transfer curves and synaptic characteristics of our S-AVSs at various strain levels. As illustrated in Fig. 3(c) and Fig. S7 in the ESM, the current of transfer curves was enhanced under optical illumination and the light-to-dark current ratio remained relatively stable at different strain states. Taking advantage of the intrinsic stretchability of all materials in S-AVS, our device demonstrates robust transfer curves under cyclic mechanical strain (Fig. S8 in the ESM). The output characteristic curves in Fig. 3(d) illustrate the device's current response to light (365 nm) at 0% and 30% strain. We chose a strain value below 30% based on the deformation limit of human skin, which is 30%, with rupture occurring at levels greater than 30% [44, 45]. Furthermore, the EPSC triggered by 450 nm light pulse (130 μW/cm², 1 s) slightly decayed as the strain increased and returned to the initial value after recovering 0% strain (Fig. 3(e) and Fig. S9 in the ESM). Importantly, after stretching to 30% for 100 cycles, the EPSC could remain at the initial value (Fig. S10 in the ESM). Even after stretching to 30% for 10,000 cycles, the EPSC behavior remain robust (Fig. S11 in the ESM). Additionally, the PPF index of S-AVS during stretching was compared to further investigate the impact on synaptic characteristics brought by strains. In Fig. 3(f), the PPF behavior can still be simulated as the stretching degree increases, and the PPF index is almost constant. To ensure the reliability of the characterization of the PPF index, the error bars were attained from three independent tests of the device. This device demonstrated robustness under mechanical strain, even repeated strain cycles, affirming its suitability for practical applications.

With the fading memory effect of aforementioned synaptic characteristics, S-AVSs could be employed to implement the RC algorithm. RC comprises a randomly arranged pool of nonlinear neurons, resulting in a simpler network structure compared to conventional neural networks. To further reflect the efficiency of designed RC vision system in addressing image classification tasks, we constructed stretchable optoelectronic RC systems to recognize the handwritten digits in the Modified National Institute of Standards and Technology database (MNIST). The fundamental principle of image recognition based on stretchable optoelectronic RC vision systems is as follows: Consider a 5 pixel × 4 pixel image, and the image is divided into 5 rows. Pixels that receive light pulses are defined as "1", while those that do not receive light pulses are defined as "0". For example, the row in which all 4 pixels are fully illuminated can be denoted the sequence "1111" (Fig. 4(a)). The number and order of light pulses received by the synaptic devices representing rows vary for different images. Consequently, optical pulse trains representing image information can be converted into straightforward EPSC values. An array of 5 × 1 devices was prepared for optical information preprocessing. Obviously, RC based on S-AVS can effectively distinguish these pulse sequences based on the final output current value (Figs. 4(b) and 4(c), and Figs. S12 and S13 in the ESM). Therefore, the RC for each digit exhibited five distinct final output current values, indicating that the reservoir constructed with our stretchable devices is capable of

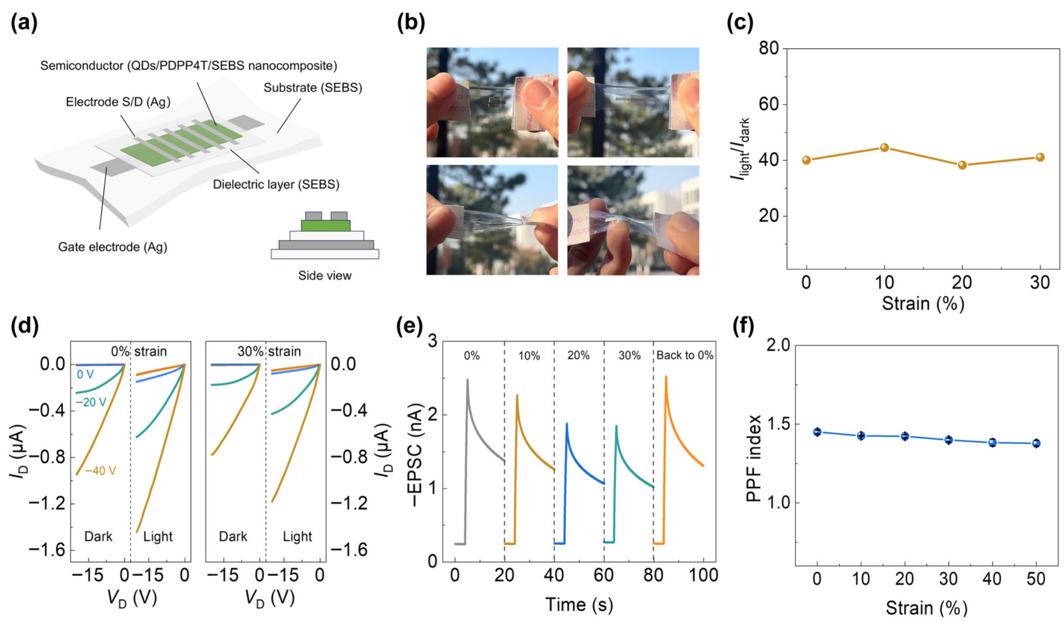

Figure 3 (a) Schematic and side view of the S-AVS. (b) Optical photographs of S-AVS under sequential stretching, twisting, and poking deformations. (c) Current ratio of S-AVS under dark and light illumination conditions (365 nm) at different stretching states. (d) Output characteristic curves of S-AVS under dark and light illumination conditions (365 nm) at 0% strain and 30% strain along the channel length direction. (e) The EPSC behavior triggered by an optical pulse (130 μW/cm², 1 s) at different stretching states along the channel length direction. (f) PPF index at different stretching states. Error bars represent standard errors attained from three independent tests of the device.

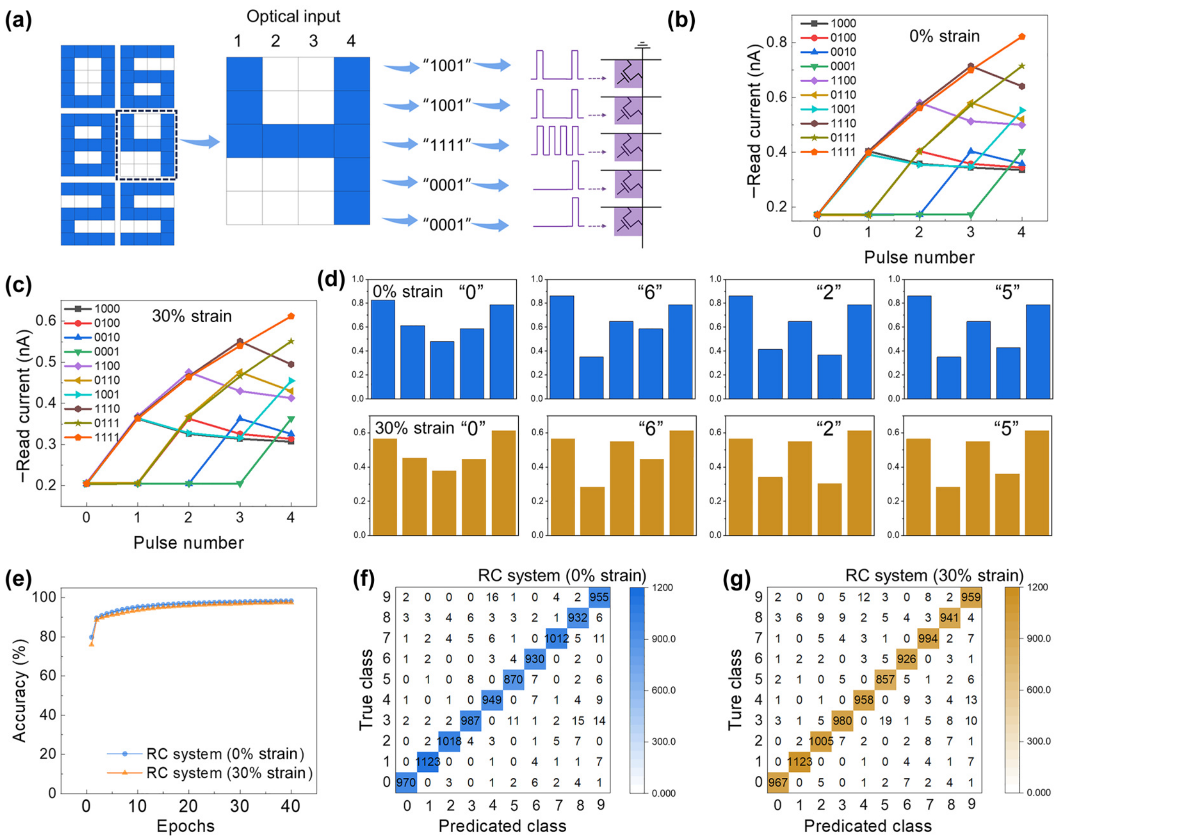

Figure 4 (a) Schematic of stretchable RC systems for image recognition. Experimental read-current responses of stretchable RC systems triggered by several optical input signals at (b) 0% strain and (c) 30% strains along the channel length direction. (d) The experimental read-current responses of stretchable RC systems constituting digits 0, 6, 2, and 5 at 0% and 30% strains. (e) The recognition accuracy of unstretched RC, and RC systems at 30% strain along the channel length direction. (f) and (g) The confusion matrix of different systems.

distinguishing ten digits by different output states (Fig. 4(d) and Fig. S14 in the ESM). The corresponding current values for each image were fed into a backend fully connected neural network for training and recognition. After 40 training epochs, the accuracy of our RC vision system reached 97.46% and 97.1% for unstretched and stretched states, respectively (Fig. 4(e)). The confusion matrix of three systems showing the classification of the handwritten digits is presented in Figs. 4(f) and 4(g). The high classification accuracy of our S-AVSs-based RC vision system holds promising application potential for next-generation intelligent systems, including ocular prostheses, robots, and autonomous vehicles, among others.

4 Conclusions

This study introduces a prototype S-AVS capable of sensing and processing optical signals while adapting to shape deformation. The S-AVSs employ a transistor structure with all components designed for stretchability, particularly emphasizing the stretchable photosensitive semiconductor layer. Various synaptic behaviors, including EPSC and PPF, are successfully demonstrated using optical signals. These functionalities remain robust even under significant deformation, enduring strains of up to 30% and repeated stretching. Additionally, the RC vision system based on S-AVSs achieved image recognition accuracies of 97.46% and 97.1% at 0% and 30% strain, respectively. The impressive classification accuracy of our S-AVSs-based RC vision system suggests promising applications in next-generation intelligent systems.

Electronic Supplementary Material: Supplementary material (schematic of the soft contact lamination method, transfer curves, photoresponsivity of devices, optical micrograph of films, AFM images, resistance of stretchable Ag electrodes, EPSC behavior, experimental read-current responses of RC systems) is available in the online version of this article at https://doi.org/10.26599/NR.2025.94907191.

Data availability

All data needed to support the conclusions in the paper are presented in the manuscript and the ESM. Additional data related to this paper may be requested from the corresponding author upon request.

Acknowledgements

This work was supported by the the Innovation Program of Shanghai Municipal Education Commission (No. 2021-01-07-00-07-E00096), the National Natural Science Foundation of China (Nos. 62074111 and 62374115) and the National Key Research and Development Program of China (No. 2022YFB3203502).

Declaration of competing interest

All the contributing authors report no conflict of interests in this work.

Author contribution statement

T. R. S.: Conducted measurements and analysis of device performances, data curation, wrote and revised manuscript. X. L.: Contributing the neuromorphic computing of handwritten image recognition. Y. T. X.: Conducted measurements and analysis of device performances, wrote manuscript. X. L. Z.: Revised manuscript. P. G.: Conducted measurements and analysis of device performances. J. Y. Z.: Conducted measurements and analysis of device performances. Z. Y. G.: Gave suggestions about the experiments. Y. W.: Conducted measurements and analysis of device performances. S. L. D.: Conceived project and supervised this project, project administration, gave suggestions about the experiments, revised manuscript. J. H.: Conceived project and supervised this project, project administration, funding acquisition, gave suggestions about the experiments, revised manuscript.

Use of AI statement

None.

References

[1] Chen, C. W. Internet of video things: Next-generation IoT with visual sensors. *IEEE Internet Things J.* **2020**, *7*, 6676–6685.

[2] Li, Y.; Moreau, J.; Ibanez-Guzman, J. Emergent visual sensors for autonomous vehicles. *IEEE Trans. Intell. Transp. Syst.* **2023**, *24*, 4716–4737.

[3] Aziz, A.; Pane, S.; Iacovacci, V.; Koukourakis, N.; Czarske, J.; Menciassi, A.; Medina-Sánchez, M.; Schmidt, O. G. Medical imaging of microrobots: Toward *in vivo* applications. *ACS Nano* **2020**, *14*, 10865–10893.

[4] Yang, J. C.; Wang, C. G.; Jiang, B.; Song, H. B.; Meng, Q. G. Visual perception enabled industry intelligence: State of the art, challenges and prospects. *IEEE Trans. Ind. Inf.* **2021**, *17*, 2204–2219.

[5] Coburn, C.; Fan, D. J.; Forrest, S. R. Organic charge-coupled device. *ACS Photonics* **2019**, *6*, 2090–2095.

[6] El Gamal, A.; Eltoukhy, H. CMOS image sensors. *IEEE Circuits Devices Mag.* **2005**, *21*, 6–20.

[7] Yokogawa, S.; Burgos, S. P.; Atwater, H. A. Plasmonic color filters for CMOS image sensor applications. *Nano Lett.* **2012**, *12*, 4349–4354.

[8] Zhang, J. Y.; Guo, P.; Guo, Z. Y.; Li, L.; Sun, T. R.; Liu, D. P.; Tian, L.; Zu, G. Q.; Xiong, L. Z.; Zhang, J. H. et al. Retina-inspired artificial synapses with ultraviolet to near-infrared broadband responses for energy-efficient neuromorphic visual systems. *Adv. Funct. Mater.* **2023**, *33*, 2302885.

[9] Zhou, F. C.; Chai, Y. Near-sensor and in-sensor computing. *Nat. Electron.* **2020**, *3*, 664–671.

[10] Gu, L. L.; Poddar, S.; Lin, Y. J.; Long, Z. H.; Zhang, D. Q.; Zhang, Q. P.; Shu, L.; Qiu, X.; Kam, M.; Javey, A. et al. A biomimetic eye with a hemispherical perovskite nanowire array retina. *Nature* **2020**, *581*, 278–282.

[11] Zhang, J. Y.; Guo, Z. Y.; Sun, T. R.; Guo, P.; Liu, X.; Gao, H. Y.; Dai, S. L.; Xiong, L. Z.; Huang, J. Energy-efficient organic photoelectric synaptic transistors with environment-friendly $CuInSe_2$ quantum dots for broadband neuromorphic computing. *SmartMat* **2024**, *5*, e1246.

[12] Zhang, J. Y.; Shi, Q. Q.; Wang, R. Z.; Zhang, X.; Li, L.; Zhang, J. H.; Tian, L.; Xiong, L. Z.; Huang, J. Spectrum-dependent photonic synapses based on 2D imine polymers for power-efficient neuromorphic computing. *InfoMat* **2021**, *3*, 904–916.

[13] Yu, H. Y.; Zhao, X. L.; Tan, M. Y.; Wang, B.; Zhang, M. X.; Wang, X.; Guo, S. L.; Tong, Y.; Tang, Q. X.; Liu, Y. C. Ultraflexible and ultrasensitive near-infrared organic phototransistors for hemispherical biomimetic eyes. *Adv. Funct. Mater.* **2022**, *32*, 2206765.

[14] Chen, H.; Hou, Y. Q.; Shi, Y. H.; Zhang, Y. C.; Wang, S.; Peng, Q.; Huang, H. Organic all-photonic artificial synapses enabled by anti-stokes photoluminescence. *J. Am. Chem. Soc.* **2023**, *145*, 11988–11996.

[15] Shan, L. T.; Chen, Q. Z.; Yu, R. J.; Gao, C. S.; Liu, L. J.; Guo, T. L.; Chen, H. P. A sensory memory processing system with multi-wavelength synaptic-polychromatic light emission for multi-modal information recognition. *Nat. Commun.* **2023**, *14*, 2648.

[16] Sun, L.; Qu, S. D.; Du, Y.; Yang, L.; Li, Y.; Wang, Z. X.; Xu, W. T. Bio-inspired vision and neuromorphic image processing using printable metal oxide photonic synapses. *ACS Photonics* **2023**, *10*, 242–252.

[17] Gao, C. S.; Yang, H. H.; Li, E. L.; Yan, Y. J.; He, L. H.; Chen, H. P.; Lin, Z. X.; Guo, T. L. Heterostructured vertical organic transistor for high-performance optoelectronic memory and artificial synapse. *ACS Photonics* **2021**, *8*, 3094–3103.

[18] Guo, Z. Y.; Zhang, J. Y.; Yang, B.; Li, L.; Liu, X.; Xu, Y. T.; Wu, Y.; Guo, P.; Sun, T. R.; Dai, S. L. et al. Organic high-temperature synaptic phototransistors for energy-efficient neuromorphic computing. *Adv. Mater.* **2024**, *36*, 2310155.

[19] Chen, Y. C.; Li, Y.; Niu, S. F.; Yang, X.; Dou, W. J.; Shan, C. X.; Shen, G. Z. High temperature resistant solar-blind ultraviolet photosensor for neuromorphic computing and cryptography. *Adv. Funct. Mater.* **2024**, *34*, 2315383.

[20] Zhu, S. R.; Xie, T.; Lv, Z. Y.; Leng, Y. B.; Zhang, Y. Q.; Xu, R. Z.; Qin, J.; Zhou, Y.; Roy, V. A. L.; Han, S. T. Hierarchies in visual pathway: Functions and inspired artificial vision. *Adv. Mater.* **2024**, *36*, e2301986.

[21] Gong, Y.; Xie, P.; Xing, X. C.; Lv, Z. Y.; Xie, T.; Zhu, S. R.; Hsu, H. H.; Zhou, Y.; Han, S. T. Bioinspired artificial visual system based on 2D WSe_2 synapse array. *Adv. Funct. Mater.* **2023**, *33*, 2303539.

[22] Zhang, Y. C.; Chen, H.; Sun, W. Q.; Hou, Y. Q.; Cai, Y. H.; Huang, H. All-photonic synapses for biomimetic ocular system. *Adv. Funct. Mater.* **2024**, *34*, 2409149.

[23] Wang, S.; Chen, H.; Liu, T. H.; Wei, Y. N.; Yao, G.; Lin, Q. J.; Han, X.; Zhang, C. F.; Huang, H. Retina-inspired organic photonic synapses for selective detection of SWIR light. *Angew. Chem., Int. Ed.* **2023**, *62*, e202213733.

[24] Wang, C. Y.; Bian, Y. S.; Liu, K.; Qin, M. C.; Zhang, F.; Zhu, M. L.; Shi, W. K.; Shao, M. C.; Shang, S. C.; Hong, J. X. et al. Strain-insensitive viscoelastic perovskite film for intrinsically stretchable neuromorphic vision-adaptive transistors. *Nat. Commun.* **2024**, *15*, 3123.

[25] Chen, J. W.; Zhou, Z.; Kim, B. J.; Zhou, Y.; Wang, Z. Q.; Wan, T. Q.; Yan, J. M.; Kang, J. F.; Ahn, J. H.; Chai, Y. Optoelectronic graded neurons for bioinspired in-sensor motion perception. *Nat. Nanotechnol.* **2023**, *18*, 882–888.

[26] Ren, Y. Y.; Bu, X. B.; Wang, M.; Gong, Y.; Wang, J. J.; Yang, Y. Y.; Li, G. J.; Zhang, M.; Zhou, Y.; Han, S. T. Synaptic plasticity in self-powered artificial striate cortex for binocular orientation selectivity. *Nat. Commun.* **2022**, *13*, 5585.

[27] Xu, F.; Zhang, C.; Zhao, X. L.; Yu, H. Y.; Zhao, G. D.; Li, J. T.; Wang, B.; Tong, Y. H.; Tang, Q. X.; Liu, Y. C. Intrinsically stretchable photonic synaptic transistors for retina-like visual image systems. *J. Mater. Chem. C* **2022**, *10*, 10586–10594.

[28] Wang, C. Y.; Liu, Y. Q.; Guo, Y. L. Intrinsically flexible organic phototransistors for bioinspired neuromorphic sensory system. *Wearable Electron.* **2024**, *1*, 41–52.

[29] Xie, T. H.; Wang, Q. N.; Li, M.; Fang, Y. X.; Li, G.; Shao, S. S.; Yu, W. B.; Wang, S. Y.; Gu, W. B.; Zhao, C. et al. Carbon nanotube optoelectronic synapse transistor arrays with ultra-low power consumption for stretchable neuromorphic vision systems. *Adv. Funct. Mater.* **2023**, *33*, 2303970.

[30] Sun, L. F.; Wang, Z. R.; Jiang, J. B.; Kim, Y.; Joo, B.; Zheng, S. J.; Lee, S.; Yu, W. J.; Kong, B. S.; Yang, H. In-sensor reservoir computing for language learning via two-dimensional memristors. *Sci. Adv.* **2021**, *7*, eabg1455.

[31] Zhang, Z. F.; Zhao, X. L.; Zhang, X. M.; Hou, X. H.; Ma, X. L.; Tang, S. Z.; Zhang, Y.; Xu, G. W.; Liu, Q.; Long, S. B. In-sensor reservoir computing system for latent fingerprint recognition with deep ultraviolet photo-synapses and memristor array. *Nat. Commun.* **2022**, *13*, 6590.

[32] Liang, X. P.; Tang, J. S.; Zhong, Y. N.; Gao, B.; Qian, H.; Wu, H. Q. Physical reservoir computing with emerging electronics. *Nat. Electron.* **2024**, *7*, 193–206.

[33] Wu, X. S.; Shi, S. H.; Liang, B. S.; Dong, Y.; Yang, R. M.; Ji, R. D.; Wang, Z. R.; Huang, W. G. Ultralow-power optoelectronic synaptic transistors based on polyzwitterion dielectrics for in-sensor reservoir computing. *Sci. Adv.* **2024**, *10*, eadn4524.

[34] Wu, X. S.; Wang, S. C.; Huang, W.; Dong, Y.; Wang, Z. R.; Huang, W. G. Wearable in-sensor reservoir computing using optoelectronic polymers with through-space charge-transport characteristics for multi-task learning. *Nat. Commun.* **2023**, *14*, 468.

[35] Xu, J.; Wang, S. H.; Wang, G. J. N.; Zhu, C. X.; Luo, S. C.; Jin, L. H.; Gu, X. D.; Chen, S. C.; Feig, V. R.; To, J. W. F. et al. Highly stretchable polymer semiconductor films through the nanoconfinement effect. *Science* **2017**, *355*, 59–64.

[36] Dai, Y. H.; Dai, S. L.; Li, N.; Li, Y.; Moser, M.; Strzalka, J.; Prominski, A.; Liu, Y. D.; Zhang, Q. T.; Li, S. S. et al. Stretchable redox-active semiconducting polymers for high-performance organic electrochemical transistors. *Adv. Mater.* **2022**, *34*, e2201178.

[37] Liu, X.; Dai, S. L.; Zhao, W. D.; Zhang, J. Y.; Guo, Z. Y.; Wu, Y.; Xu, Y. T.; Sun, T. R.; Li, L.; Guo, P. et al. All-photolithography fabrication of ion-gated flexible organic transistor array for multimode neuromorphic computing. *Adv. Mater.* **2024**, *36*, 2312473.

[38] Wu, Y.; Dai, S. L.; Liu, X.; Guo, P.; Zhang, J. Y.; Sun, T. R.; Guo, Z. Y.; Xu, Y. T.; Liang, H. X.; Xiong, L. Z. et al. Optical microlithography of perovskite quantum dots/organic semiconductor heterojunctions for neuromorphic photosensors. *Adv. Funct. Mater.* **2024**, *34*, 2315175.

[39] Kavalali, E. T. The mechanisms and functions of spontaneous neurotransmitter release. *Nat. Rev. Neurosci.* **2015**, *16*, 5–16.

[40] Gao, Y. S.; Zhang, J. Y.; Liu, D. P.; Sun, T. R.; Wang, J.; Li, L.; Dai, S. L.; Zhang, J. H.; Yang, Z. L.; Huang, J. Artificial synapses based on organic electrochemical transistors with self-healing dielectric layers. *Chin. Chem. Lett.* **2024**, *35*, 108582.

[41] Hua, Z. K.; Yang, B.; Zhang, J. Y.; Hao, D. D.; Guo, P.; Liu, J.; Jiang, L.; Huang, J. Monolayer molecular crystals for low-energy consumption optical synaptic transistors. *Nano Res.* **2022**, *15*, 7639–7645.

[42] Guo, P.; Zhang, J. Y.; Liu, D. P.; Wang, R. Z.; Li, L.; Tian, L.; Huang, J. Optoelectronic synaptic transistors based on solution-processable organic semiconductors and $CsPbCl_3$ quantum dots for visual nociceptor simulation and neuromorphic computing. *ACS Appl. Mater. Interfaces* **2023**, *15*, 51483–51491.

[43] Kim, M. H.; Jeong, M. W.; Kim, J. S.; Nam, T. U.; Vo, N. T. P.; Jin, L. H.; Lee, T. I.; Oh, J. Y. Mechanically robust stretchable semiconductor metallization for skin-inspired organic transistors. *Sci. Adv.* **2022**, *8*, eade2988.

[44] Webb, R. C.; Bonifas, A. P.; Behnaz, A.; Zhang, Y. H.; Yu, K. J.; Cheng, H. Y.; Shi, M. X.; Bian, Z. G.; Liu, Z. J.; Kim, Y. S. et al. Ultrathin conformal devices for precise and continuous thermal characterization of human skin. *Nat. Mater.* **2013**, *12*, 938–944.

[45] Tavakoli, M.; Malakooti, M. H.; Paisana, H.; Ohm, Y.; Marques, D. G.; Alhais Lopes, P.; Piedade, A. P.; De Almeida, A. T.; Majidi, C. EGaIn-assisted room-temperature sintering of silver nanoparticles for stretchable, inkjet-printed, thin-film electronics. *Adv. Mater.* **2018**, *30*, 1801852.